PAPER

Check for updates

Mo-doped TiO₂ photoanodes using [Ti₄Mo₂O₈(OEt)₁₀]₂ bimetallic oxo cages as a single source precursor†

Miriam Regue, [iD] [ab] Katherine Armstrong, [c] Dominic Walsh, [iD] [b] Emma Richards, [iD] [c] Andrew L. Johnson [iD] [ad] and Salvador Eslava [iD] *[ab]

Photoelectrochemical solar water splitting is a promising and sustainable technology for producing solar fuels such as clean hydrogen from water. A widely studied photoanode semiconductor for this application is TiO₂, but it suffers from a large band gap (3.2 eV) and fast recombination of electrons and holes. Herein, we present a novel, facile and rapid strategy to develop Mo-doped TiO₂ (Mo:TiO₂) mixed anatase–rutile photoanodes using [Ti₄Mo₂O₈(OEt)₁₀]₂ bimetallic oxo cages as a single source precursor. These cages dissolved in tetrahydrofuran deposit by spray pyrolysis at 150 °C forming films with hierarchical porosity on the micrometer and nanometer scale. XPS, EDXS and UV-Vis spectroscopy reveal Mo atoms evaporate during annealing in air at temperatures 650–800 °C, contributing to the formation of nanostructures and porosity. XPS depth profiling, XRD, EDXS, Raman, and electron paramagnetic resonance indicate that the remaining Mo atoms are well spread and incorporated in the TiO₂ lattice, at interstitial or substitutional sites of the rutile or anatase phases depending on the annealing temperature. Photocurrent measurements show that Mo:TiO₂ photoanodes optimized at 700 °C outperform a TiO₂ photoanode prepared in a similar manner by a factor of two at 1.23 V_{RHE}. Finally, UV-Vis spectroscopy, conduction and valence band calculations, and incident-to-photon efficiency measurements show these Mo:TiO₂ photoanodes possess a narrower band gap than TiO₂ and higher efficiency in the visible light range (5% at 400 nm). These outcomes open a new avenue in the exploitation of titanium oxo cages and advance the development of photoelectrodes for water splitting and energy applications.

1. Introduction

The abundant solar energy, 1.3×10^5 TW per year reaching the Earth's surface, can be utilized to produce hydrogen fuel by splitting water, offering an excellent and sustainable alternative to fossil fuels. Among solar absorber candidates in photoelectrochemical (PEC) solar water splitting devices, TiO₂ is one of the most promising ones due to its chemical and thermal stability, long durability, excellent optical and electronic properties, low cost and non-toxicity.[1–3] However, TiO₂-based PEC cells are still far from commercialization mainly due to both fast recombination of photogenerated electrons and holes in TiO₂

and its large band gap (3.2 eV for the anatase phase) that results in a reduced use of the solar spectrum. One strategy to overcome its limitations is doping it with transition metals. The metal doping increases the solar light absorption of TiO₂ and performance by incorporating additional energy levels within the band gap of the semiconductor.[4,5] Nevertheless, this only seems to occur when there is an actual substitution of Ti atoms in the TiO₂ lattice structure with the external metal (known as substitutional doping), that reduces the band gap of the material without compromising the surface of the photocatalyst.[6] Otherwise, if metals are simply impregnated on the surface of the semiconductor they may result in electron–hole recombination and blocking of reaction sites.[6,7]

Research on metal doping of TiO₂ with Ta, Fe, Co, Mn, and Ni is abundant and has proved to be successful in both reducing the band gap and improving the photoelectrochemical performance (PEC).[8–11] For instance, Yan *et al.* reported an enhancement in the PEC performance for Ta-doped TiO₂ nanotube photoanodes in comparison to pristine TiO₂.[8] This enhanced PEC performance was attributed to a decrease in the band gap, lower charge transfer resistance and higher charge carrier density. Similarly, Zhao *et al.* successfully demonstrated that Fe-

ᵃCentre for Sustainable Chemical Technologies, University of Bath, Claverton Down, Bath, BA2 7AY, UK. E-mail: S.Eslava@bath.ac.uk

ᵇDepartment of Chemical Engineering, University of Bath, Claverton Down, Bath, BA2 7AY, UK

ᶜSchool of Chemistry, Cardiff University, Main Building, Park Place, Cardiff CF10 3AT, UK

ᵈDepartment of Chemistry, University of Bath, Claverton Down, Bath, BA2 7AY, UK

† Electronic supplementary information (ESI) available: All data created during this research are openly available from the University of Bath data archive at https://doi.org/10.15125/BATH-00437. See DOI: 10.1039/c8se00372f

doped TiO_2 results in a better PEC performance than pristine TiO_2, attributed to a smaller band gap and thus a better light absorption.[9] However, very few studies have been reported for Mo doping of TiO_2 and those few were mainly focused on photodegradation of organic dyes, not PEC water splitting.[12–16] In 2015 Zhang et al. reported Mo-doped TiO_2 photoanodes prepared using two steps of Ti foil anodization and a third one of hydrothermal doping, obtaining an improved PEC performance over pure TiO_2 photoanodes.[17] The improvement was attributed to a decrease in the recombination of electrons and holes in the mixed phase of anatase and rutile and to better light absorption.

Heterometallic titanium oxo (HMTO) cages such as $[Ti_xO_y (L)_zM_nX_m]$, where L is a ligand, M a metal and X a halide, can be prepared with a wide range of metal compositions (e.g. with M = Co, Ni, and Mo), nuclearities, spatial arrangements, and functionalities via simple solvothermal methods and isolated by crystallization.[18–23] Some of these cages, also called clusters, have successfully been used as precursors for photocatalysts or electrocatalysts, for example using graphene oxide as a sacrificial template or impregnating WO_3 photoanodes.[20,24] However, their wide adoption as single source precursors still requires finding facile and effective approaches that overcome their instability in water or humid environments.

In this publication, we report for the first time a facile and rapid synthesis of porous Mo-doped TiO_2 photoanodes using a $[Ti_4Mo_2O_8(OEt)_{10}]_2$ HMTO cage as a single source precursor. Stability of the cages during the deposition is ensured using anhydrous tetrahydrofuran as solvent and spray pyrolysis as deposition method. We reveal that upon deposition, the calcination at temperatures above 600 °C induces sublimation of Mo atoms adding porosity and nanostructured features to remaining TiO_2, while the rest of Mo atoms effectively occupy substitutional or interstitial sites in the TiO_2 lattice. The resulting Mo:TiO_2 photoanode optimized at 700 °C outperforms by a factor of two a pure TiO_2 photoanode prepared in a similar manner in PEC solar water splitting. The results herein presented therefore reveal new strategies to develop efficient photoelectrodes for water splitting applications using Mo as both a sacrificial agent and dopant and opens an avenue to exploit HMTO cages as single source precursors using spray pyrolysis.

2. Experimental

Materials

Titanium(IV) ethoxide $[Ti(OEt)_4]$, anhydrous molybdenum(V) chloride ($MoCl_5$, 99.99%), anhydrous tetrahydrofuran (≥99.9%, inhibitor free), anhydrous ethanol (<0.0003% water), titanium isopropoxide (TTIP, 97%), acetylacetone (AcAc), cobalt nitrate ($Co(NO_3)_2$), iron chloride hexahydrate ($FeCl_3·6H_2O$), sodium acetate (NaOAc) and tetrabutylammonium hexafluorophosphate ($TBAPF_6$) were provided by Sigma Aldrich. Cobalt(II) chloride ($CoCl_2$, anhydrous 97%) was provided by Alfa Aesar. Aluminoborosilicate glass (ABS) coated with fluorine-doped tin oxide (FTO) transparent conductive layer (8 Ω sq^{-1}) was provided by Solaronix, SA. These FTO-ABS substrates were cleaned ultrasonically in a 2% aqueous Hellmanex III solution

followed by dipping in deionized water, acetone and isopropyl alcohol, ultrasonicating in each step for 3 min. Finally, the substrates were rinsed with deionized water and dried with compressed air.

Synthesis of $[Ti_4Mo_2O_8(OEt)_{10}]_2$

$[Ti_4Mo_2O_8(OEt)_{10}]_2$ oxo cages (Fig. 1) were synthesized using a solvothermal process as described in a previous article by Eslava et al.[25] Briefly, $Ti(OEt)_4$ (14 mL, 66.8 mmol), $MoCl_5$ (1.128 g, 4.12 mmol) and anhydrous ethanol (14 mL) were carefully mixed in a 45 mL Teflon-lined stainless steel autoclave and heated to 150 °C for 24 hours. The autoclave was left overnight to cool down to room temperature and mm size brown-red crystals were obtained (88% yield). Elemental analysis (%) calculated for $C_{40}H_{100}Mo_4O_{36}Ti_8$: C 25.7, H 5.3; found: C 25.6, H 5.3. Due to the sensitive nature of these reactants, all manipulations were carried out in an air-free atmosphere involving the use of a glove box and Schlenk line when necessary.

Preparation of Mo:TiO_2 and TiO_2 films

Mo-doped TiO_2 (abbreviated as Mo:TiO_2) and pure TiO_2 films to be studied as photoanodes were prepared using a manual spray-pyrolysis system (Clarke CAB3P) on FTO-ABS. The solutions employed for the spray pyrolysis deposition were prepared in an argon atmosphere using a Schlenk line. Nevertheless, the actual spray pyrolysis deposition process was conducted in air, but vessels were kept closed when possible. The precursor solution for the Mo:TiO_2 photoanodes was prepared by dissolving $[Ti_4Mo_2O_8(OEt)_{10}]_2$ (0.96 g) in anhydrous tetrahydrofuran (20 mL). The precursor solution for the preparation of pure TiO_2 was carried out following an established method.[26] Briefly, a 0.2 M solution of TTIP was prepared by diluting TTIP and AcAc in a 3 : 2 volumetric ratio and topping up with absolute ethanol in order to obtain 0.2 M solution of TTIP.

The spray pyrolysis deposition of previous precursor solutions to prepare Mo:TiO_2 and TiO_2 photoanode films was conducted as follows. In a first stage, FTO-ABS was pre-heated on a hot plate at 150 °C. Secondly, the as-prepared precursor solutions were sprayed on top of the pre-heated FTO-ABS, at
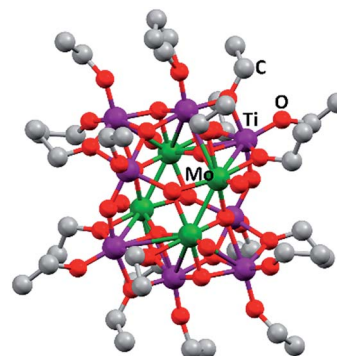

Fig. 1 Ball and stick drawing of $[Ti_4Mo_2O_8(OEt)_{10}]_2$ represented from CCDC no. 812604.[25] Mo: green; Ti: purple; O: red; C: grey.

a constant distance of *ca.* 5 cm from the surface of the FTO-ABS to the spray pyrolysis nozzle. Three deposition layers were performed per sample. Finally, the as-prepared Mo:TiO$_2$ and TiO$_2$ films were annealed at different temperatures between 450 and 800 °C for 2 h in air at a ramp rate of 10 °C min^{-1}. This range of temperatures was chosen to ensure full conversion of the precursor to the metal oxide and to evaluate the effect that different annealing conditions might have on the photoanode performance. The resultant photoanodes were denoted as Mo:TiO$_2$-### and TiO$_2$-###, where ### is the corresponding annealing temperature (°C).

Cobalt phosphate (Co-P$_i$) loading on Mo:TiO$_2$-700 photoanodes was carried out by photo-electrodeposition.[27,28] The electrolyte consisted of 0.05 mM of cobalt nitrate in 0.1 M potassium phosphate buffer (pH = 7) and the applied potential 1 V$_{RHE}$ was kept for 20 s under simulated sunlight (AM 1.5G, 100 mW cm^{-2}) from a filtered 300W Xenon lamp source. Illumination was directed towards the back of the FTO-ABS working electrode. CoFeO$_x$ was deposited on Mo:TiO$_2$-700 by electrodeposition.[29] The electrolyte consisted of 10 mM FeCl$_3$·6H$_2$O, 16 mM CoCl$_2$ and 0.1 M NaOAc dissolved in deionized water. The pH of the solution was 4.90. The deposition was carried out by positively sweeping the voltage from 1.1 to 1.4 V$_{Ag/AgCl}$ three times. In both depositions, a Compactstat. potentiostat (Ivium Technologies) was used and an electrochemical cell consisting of a Pt counter electrode, a silver chloride (Ag/AgCl/3.5 M KCl) reference electrode, and a Mo:TiO$_2$-700 photoanode as working electrode.

Characterization

^{13}C NMR spectroscopy was conducted at room temperature using a 500 MHz Agilent Propulse spectrophotometer. Samples were dissolved in dried deuterated benzene (C$_6$d$_6$). Elemental analysis was performed on a Carlo Erba Flash 2000 Elemental Analyser. Field emission scanning electron microscopy images (FE-SEM) were acquired using a JEOL FESEM6301F and energy dispersive X-ray spectroscopy (EDXS) was carried out in a SEM 6480LV equipped with a high sensitivity Oxford INCA X-Act SDD X-ray detector. X-Ray diffraction (XRD) patterns were collected in the 2 theta range 10–80° with a Bruker AXS D8 Advance using Cu Kα (0.154 nm) radiation with a total integration time of 960 s. Raman spectroscopy was carried out on a Renishaw inVia system using a 532 nm diode-pumped solid state laser (DPSS) manufactured by Cobolt. The laser beam was focused onto the sample using a 50× long distance objective. X-Ray photoelectron spectroscopy (XPS) depth profiling was performed using a ESCALAB 250 Xi instrument manufactured by Thermo Fisher Scientific. Measurements were carried out using a monochromated Al Kα X-ray source with an energy of 1486.68 eV. The X-ray spot size was of 900 μm and the pass energy for the high resolution scans was of 50 eV. The depth profile for the sample was obtained by etching the surface of the sample with an Ar$^+$ ion gun (2000 eV, high current) for different times (0, 60, 180 and 420 s). C 1s XPS spectra was used as an internal charge correction. Samples studied *via* electron paramagnetic resonance (EPR) spectroscopy were evacuated at 393 K for over 12 h

to reduce the influence of physisorbed water. Samples were maintained under static vacuum (10^{-5} mbar) for the duration of the experiments. For EPR analysis, powder samples were prepared by drying and calcining in air at 650, 700 and 800 °C in a porcelain dish a solution of 0.96 g of [Ti$_4$Mo$_2$O$_8$(OEt)$_{10}$]$_2$ in 20 mL of anhydrous tetrahydrofuran. High resolution transmission electron microscopy (HRTEM) images were obtained using a JEOL JEM-2100Plus microscope. Ultraviolet–visible (UV-Vis) spectra were collected in a Cary 100 diffuse reflectance UV-Vis spectrophotometer.

(Photo)Electrochemical measurements

(Photo)electrochemical performance of photoanodes was evaluated using a CompactStat. potentiostat (Ivium Technologies). Photocurrents were measured under simulated sunlight (AM 1.5G, 100 mW cm^{-2}) from a filtered 300W Xenon lamp source (Lot Quantum Design) or under UV illumination (365 nm, 3.6 mW cm^{-2}) from a ModuLight IM3412 LED light (Ivium Technologies). PEC cells consisted of three electrodes with Pt as the counter electrode, silver chloride (Ag/AgCl/3.5 M KCl) as the reference electrode and as-prepared photoanodes as the working electrodes.

Electrochemically active surface area (ECSA) of photoanodes was investigated using cyclic voltammetry (CV), scanning from 0 to 0.17 V$_{Ag/AgCl}$ at scan rates between 10 and 250 mV s^{-1}, in 1 M KOH solution (pH = 13.7). ECSA is proportional to the double layer capacitance (C$_{dl}$), which is estimated from the slope of the plot Δj *vs.* scan rate and dividing by two.[30] Δj is equal to (j_a–j_c), where j_a and j_c are the anodic and cathodic current densities, respectively, in this case taken at 0.1 V$_{Ag/AgCl}$ in the CV scans.[31]

Conduction and valence band (CB & VB) positions were measured from CV curves recorded in acetonitrile containing 0.1 M of tetrabutylammonium hexafluorophosphate (TBAPF$_6$) at a scan rate of 50 mV s^{-1} and using the following formula:[32–34]

$$\text{CB (or VB) (eV)} = -4.8 - (E - E_{1/2}) \qquad (1)$$

where E is the onset of the redox potential and $E_{1/2}$ is the formal potential of Fc/Fc$^+$ system (0.43 V$_{Ag/AgCl}$).[35]

Photoelectrochemical performances of photoanodes were carried out in a 1 M KOH (pH = 13.7) electrolyte solution. Illumination was directed towards the back of the FTO-ABS working electrode and a mask was placed on top of the photoelectrode to define the illuminated area. Photocurrent–time curves were performed at an applied bias of 1.23 V *vs.* the reversible hydrogen electrode (V$_{RHE}$). Photocurrent–potential curves were recorded at a scan rate of 20 mV s^{-1}. The measured Ag/AgCl potentials ($E_{Ag/AgCl}$) were converted to RHE potentials (E°_{RHE}) following the Nernst equation:

$$E^{\circ}_{RHE} = E^{\circ}_{Ag/AgCl} + E_{Ag/AgCl} + 0.059 \text{ pH} \qquad (2)$$

where $E^{\circ}_{Ag/AgCl}$ is 0.205 V at 25 °C (3.5M KCl). Photoelectrochemical impedance spectroscopy (PEIS) was carried out under simulated sunlight (AM 1.5G, 100 mW cm^{-2}) at a direct current (DC) potential of 1.23 V$_{RHE}$ and an alternating current

(AC) potential frequency range of 100 000–0.01 Hz with an amplitude of 5 mV. Incident photon-to-current efficiency (IPCE) measurements were calculated using the same Xe light source and a triple grating Czerny–Turner monochromator. The intensity of monochromatic light was measured at the working electrode position with SEL033/U photodetector (International Light Technologies). The following equation was used to calculate the IPCE values:[36]

$$\text{IPCE } (\lambda) = \frac{|j \text{ (mA cm}^{-2})| \times 1239.8 \text{ (V nm)}}{P_{\text{mono}} \text{ (mW cm}^{-2}) \times \lambda \text{ (nm)}} \qquad (3)$$

where j is the photocurrent density measured under single wavelength (λ) light illumination and P_{mono} is the incident irradiation power. Oxygen (O_2) measurements were conducted using a Pyroscience FireStingO2 fibre-optic oxygen meter combined with a TROXROB10 oxygen probe, together with a TDIP temperature sensor to give automatic compensation for minor fluctuation in the PEC cell temperature. O_2 readings were recorded every 10 min for ca. 410 min. The probe was fitted into the headspace of the airtight PEC cell. The PEC cell was purged with a N_2 flow to ensure air O_2 removal before the irradiation started. The measurements were carried out under simulated sunlight (AM 1.5G, 100 mW cm^{-2}) with an applied bias of 1.23 V_{RHE}. Light was irradiated for 340 min. The faradaic efficiency was calculated by dividing the measured amount of evolved O_2 by the theoretical amount of expected O_2 for measured photocurrents (assuming 100% faradaic efficiency). See more details in ESI.†

3. Results and discussion

The synthesis of $[\text{Ti}_4\text{Mo}_2\text{O}_8(\text{OEt})_{10}]_2$ cages was successfully performed using a solvothermal synthesis. The ^{13}C NMR spectra of the product showed the ten characteristic sharp resonances of the cage at δ 75.24, 75.12, 73.80, 73.49, 73.38, 73.30, 72.65, 71.67, 71.22 and 70.06 ppm belonging to the different –OCH$_2$– environments in the structure, in agreement with literature (Fig. S1, ESI†).[25] In addition, CHN elemental analysis further confirmed the successful formation of $[\text{Ti}_4\text{Mo}_2\text{O}_8(\text{OEt})_{10}]_2$ (wt% calculated for $C_{40}H_{100}Mo_4O_{36}Ti_8$: C 25.7, H 5.3; found: C 25.6, H 5.3). Fig. 1 shows a ball and stick model of the cage, which highlights a heterometallic oxo core with four Mo^V atoms in a rectangle and eight Ti^{IV} atoms. Mo and Ti atoms bridge together by a combination of μ_3-, μ_4-O and μ_2-OEt (CCDC no. 812604).

Spray pyrolysis was used to deposit solutions of $[\text{Ti}_4\text{Mo}_2\text{O}_8(\text{OEt})_{10}]_2$ cages or titanium isopropoxide-acetylacetone (TTIP-AcAc), respectively. The as-deposited films were then annealed in air at temperatures between 450 and 800 °C for 2 hours and allowed to cool to room temperature. The morphology of the as-prepared films was evaluated using SEM. Fig. 2 shows SEM images at different magnifications of Mo:TiO$_2$ prepared at different annealing temperatures (650, 700 and 800 °C), along with a film prior to calcination for comparison (i.e. a film of $[\text{Ti}_4\text{Mo}_2\text{O}_8(\text{OEt})_{10}]_2$ cages deposited by spray pyrolysis at 150 °C). At lower magnification (Fig. 2, 1st row), all Mo:TiO$_2$ films, even

the un-annealed sample, exhibit almost the same morphology, showing aggregated islands evenly distributed on top of FTO-ABS support. At slightly higher magnification (Fig. 2, 2nd row), a large amount of micrometer cavities on Mo:TiO$_2$ films are observed. These cavities contribute to an increase of surface area, which in turn must result in more active sites for the PEC oxygen evolution reaction. At even higher magnification (Fig. 2, 3rd row), it can be observed that well-defined nanostructures form as the annealing temperature increases. A highly smooth and fine surface is present before calcination (Fig. 2i), but after calcination, grain-rice-shaped nanostructures appear creating nanometer-size porosity and extra surface area (Fig. 2j–l).

SEM images of the pure TiO$_2$ film at different magnifications are shown in Fig. S2 (ESI†). Unlike Mo:TiO$_2$ films, TiO$_2$-650 (prepared with TTIP-AcAc) does not show either the presence of cavities nor nanostructures. This comparison therefore reveals the benefits of using $[\text{Ti}_4\text{Mo}_2\text{O}_8(\text{OEt})_{10}]_2$ cages as a precursor. Their decomposition and transformation to Mo-doped TiO$_2$ during the spray pyrolysis and posterior calcination leads to the formation of cavities, nanostructures and porosity. Cavities must result from the drying step upon spray pyrolysis at 150 °C. More cavities may form during the calcination and oxidation of the cages' carbon content up to 400–500 °C. Above this temperature, the grain-rice-shaped nanostructures and its associated porosity must result from the sintering of TiO$_2$ and especially from the very likely sublimation of Mo atoms. Previous reports have shown that MoO$_3$ sublimes above 700 °C.[37] The sublimation of Mo atoms was confirmed by atomic quantification from XPS data (Fig. 3a). The amount of Mo in the films decreased with temperature. For example, at the top surface (XPS-etching time 0 s) it went from 10.6 at% for Mo:TiO$_2$-650 to 4.9 and 4.3 at% for Mo:TiO$_2$-700 and Mo:TiO$_2$-800, respectively, indicating Mo sublimes within the temperatures of study. Accordingly, the percentage of carbon (C) decreases with temperature and that of Ti increases. Carbon is present from solvents and cage ethoxides and deposition of volatile organic compounds during storage. The Mo sublimation was further confirmed by an experiment of simply heating MoCl$_5$ up to 700 °C in air, which showed its complete sublimation. Therefore, Mo atoms work as pore formers, sacrificial agents that increase the porosity in the films and allow their nanostructuring.

The XPS depth profiling indicated that Mo is homogeneously distributed at different depths, but some gradient is formed at highest temperatures of 700 and 800 °C, with more C and Mo present at the surface (Fig. 3a). This may result from the gasification and sublimation taking place and accumulation at the top during the process.

ECSA measurements are shown in Fig. 3b and the corresponding CV curves in Fig. S3 (ESI†). In such measurements, the slope of the current density vs. scan rate can be related to the double layer capacitance, which is directly proportional to the ECSA.[31] Based on the obtained results, Mo:TiO$_2$-700 possesses the highest surface area ($C_{\text{dl}} = 0.10$ mF cm^{-2}), whereas TiO$_2$-650 is the sample with the smallest surface area ($C_{\text{dl}} = 0.01$ mF cm^{-2}). These results agree well with SEM images, where grain-rice-shaped nanostructures and porosity are observed for
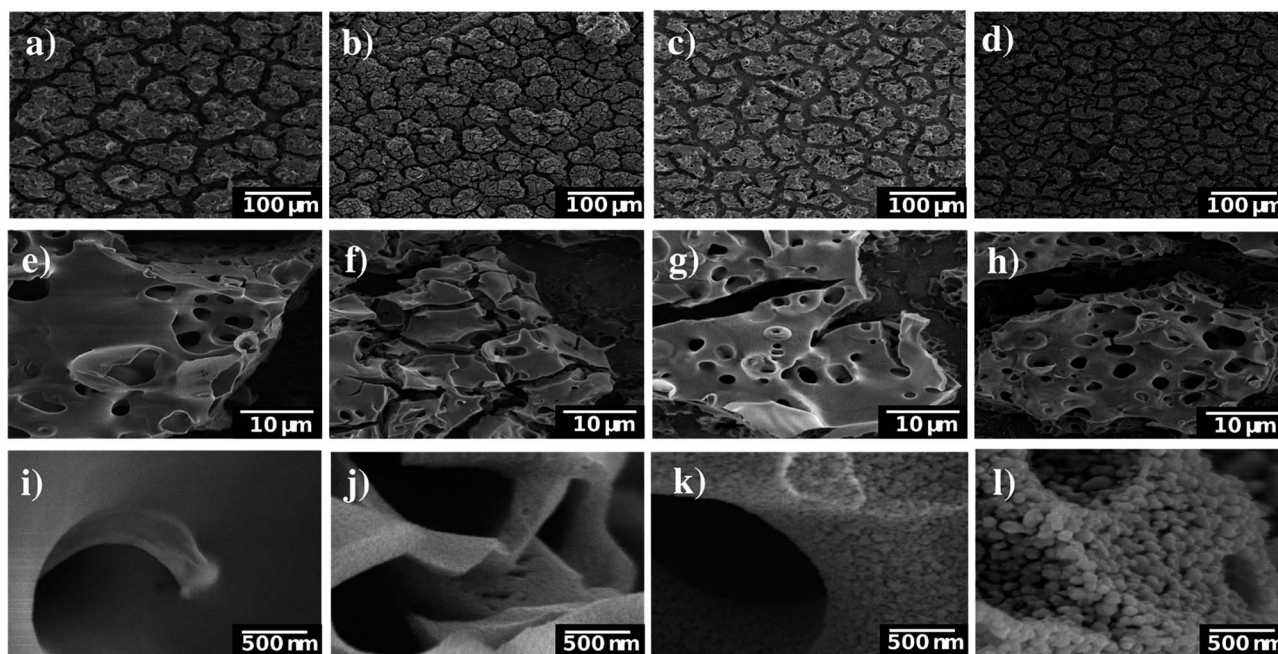
Fig. 2 SEM images of Mo:TiO$_2$ at different magnifications. (a, e and i) Film after spray-pyrolysis deposition at 150 °C, (b, f and j) Mo:TiO$_2$-650, (c, g and k) Mo:TiO$_2$-700 and (d, h and l) Mo:TiO$_2$-800.

Mo:TiO$_2$-700 (Fig. 2k) and very flat films for TiO$_2$-650 (Fig. S2, ESI†). Among all Mo:TiO$_2$ photoanodes, Mo:TiO$_2$-800 is the sample with the smallest surface area, due to the largest grains formed at highest temperature (Fig. 2l).

SEM-EDXS analysis was also carried out to evaluate the distribution of Ti, O and Mo atoms at the surface of the films. Fig. S4 (ESI†) reveals a uniform distribution of Ti and Mo atoms at the surface of Mo:TiO$_2$-650 and Mo:TiO$_2$-700. The amount of Mo atoms at the surface of Mo:TiO$_2$-800 is considerably lower supporting the hypothesis that Mo species sublime during the calcination.

Fig. 4a and b show the XRD patterns of the resulting Mo:TiO$_2$ and TiO$_2$ films on FTO-ABS. Mo:TiO$_2$-650 and Mo:TiO$_2$-700 exhibit diffraction peaks corresponding to both anatase TiO$_2$ and rutile TiO$_2$. The diffraction peaks at 2θ 25.3 and 48.0° are indexed to the diffraction planes (1 0 1) and (2 0 0) of anatase TiO$_2$, respectively (ICDD-JCPDS no. 75-1537). The diffraction peaks at 2θ 27.4, 36.1, 39.2, 44.0, 54.3, 69.0 and 69.8° correspond to (1 1 0), (1 0 1), (2 0 0), (2 1 0), (2 1 1), (3 0 1) and (1 1 2) diffraction planes, resp., of rutile TiO$_2$ (ICDD-JCPDS no. 88-1173). The diffraction of the rutile phase increases and that of anatase decreases with annealing temperature (Fig. 4a), indicating that the conversion of anatase to rutile was promoted at highest temperatures.[38] Actually, Mo:TiO$_2$-800 only shows diffraction peaks indexed to rutile TiO$_2$, due to the high calcination temperature employed. No diffraction peaks corresponding to any Mo phase such as MoO$_3$ are observed in any of the samples, which suggests that Mo$^{6+/5+}$ could be incorporated
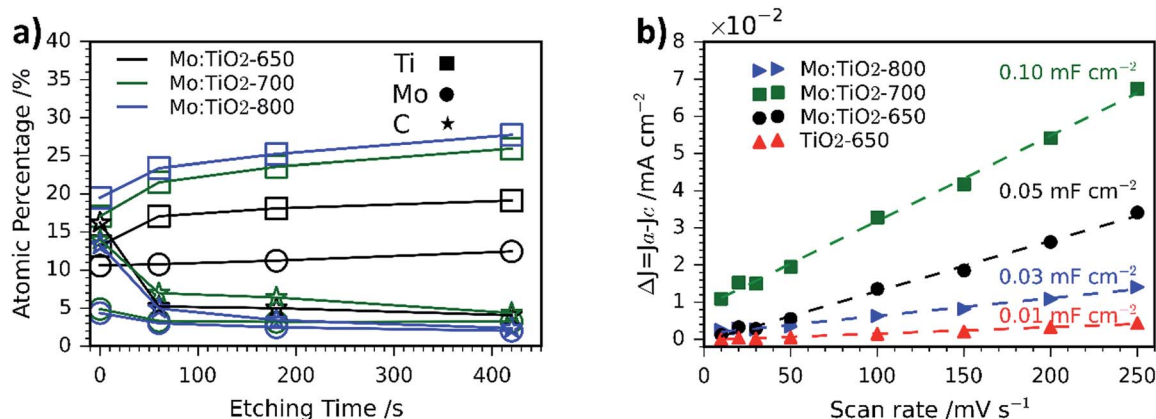

Fig. 3 (a) Atomic percentage (at%) distribution of Ti, Mo and C obtained *via* XPS depth profiling. (b) Capacitive current Δj *versus* scan rate curves of Mo:TiO$_2$ and TiO$_2$-650.
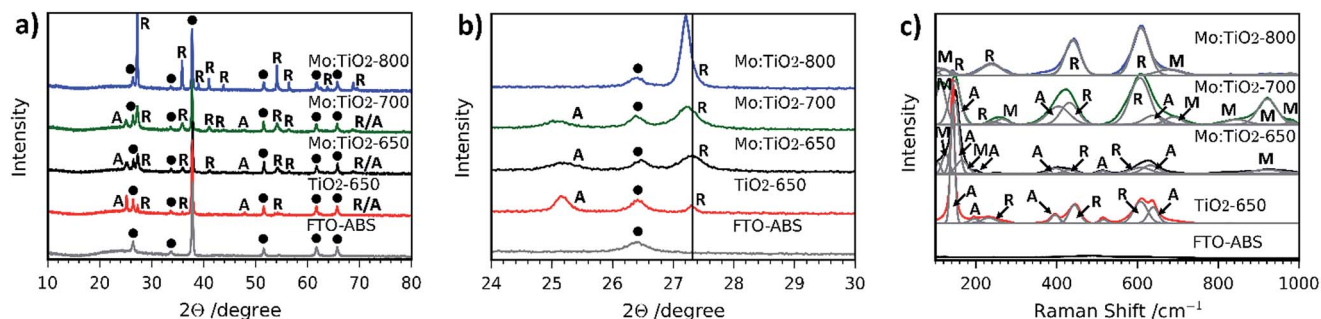
Fig. 4 (a) XRD patterns and (b) XRD diffraction profiles on (101) plane of anatase TiO_2 and (1 1 0) plane of rutile TiO_2 of Mo:TiO_2, TiO_2-650 and FTO-ABS substrate. A: anatase, R: rutile and black dot: FTO. (c) Raman spectra from 100 to 1000 cm^{-1} of Mo:TiO_2, TiO_2-650 and FTO-ABS substrate. A: anatase, R: rutile, M: Mo.

into the lattice of TiO_2. MoO_2 was unlikely to be formed since phase transformation from tetragonal MoO_2 to orthorhombic MoO_3 occurs at temperatures above 350 °C.[39]

In Fig. 4b an expansion of the (1 0 1) and (1 1 0) diffraction peaks of anatase and rutile, respectively, of the different Mo:TiO_2 and pure TiO_2 films is shown. A shift of the anatase and rutile diffraction peaks towards lower angles for Mo:TiO_2-700 and Mo:TiO_2-800 in comparison to pure TiO_2 is observed, which indicates incorporation of Mo^{6+} or Mo^{5+} atoms in the TiO_2 lattice structure upon exposure to those temperatures.[13] The reported ionic radius for Mo^{6+} and Mo^{5+} are 0.0620 and 0.0610 nm, respectively, whereas the Ti^{4+} ionic radius is 0.0605 nm.[13,40,41] The similarity in the ionic radius of these ions facilitates the aliovalent substitution of Ti^{4+} atoms for $Mo^{6+/5+}$ in the TiO_2 lattice, and due to the slightly larger size of $Mo^{6+/5+}$ in comparison to Ti^{4+} a shift in the diffraction pattern towards lower angles is observed. However, Mo:TiO_2-650 shows a smaller shift towards lower angles, suggesting that at lower temperatures the majority of $Mo^{6+/5+}$ atoms are not occupying Ti^{4+} sites in the TiO_2 lattice structure. Instead, $Mo^{6+/5+}$ must be distributed on the surface of TiO_2 or occupying interstitial sites within the TiO_2 lattice, without distorting the crystal structure of either anatase or rutile TiO_2. In fact, this may also suggest that Mo^{6+} atoms could be present in the form of MoO_3 that could be either highly dispersed on the TiO_2 surface or of amorphous structure, and therefore not detectable by XRD analysis.

Raman spectroscopy was also carried out to further verify the presence of rutile TiO_2, anatase TiO_2 and the substitution of Mo for Ti atoms in the lattice structure of TiO_2. Fig. 4c shows the Raman spectra of all films. The presence of anatase-TiO_2 and rutile-TiO_2 is confirmed by the sharp peaks observed in all Raman spectra, with the exception of Mo:TiO_2-800 for which only rutile TiO_2 is observed, in agreement with the XRD patterns (Fig. 4a and b). The sharp bands at *ca.* 145, 395, 515 and 635 cm^{-1} correspond to Raman active modes of anatase TiO_2 and bands at 230, 445 and 610 cm^{-1} to Raman active modes of rutile TiO_2.[42,43] Interestingly, some bands ascribed to the presence of Mo are also observed. For instance, in the region between 870–970 cm^{-1} there are bands belonging to hydrated terminal Mo–O and Mo–O–Mo vibrations.[44,45] The presence of

crystalline MoO_3 can be discarded since its characteristic main bands at 996, 820 and 666 cm^{-1} are not observed, which is in accordance with XRD analysis. Moreover, the weak bands observed in the range 100–200 cm^{-1} are attributed to bending modes of Mo–O–Mo.[46] This verifies the incorporation of Mo atoms into the lattice of TiO_2, suggesting the presence of Ti–O–Ti, Mo–O–Mo and Mo–O–Ti bonds in Mo:TiO_2.[47] The Mo Raman vibrations are most evident for Mo:TiO_2-700 and drastically decrease for Mo:TiO_2-800, indicating that at 700 °C the Mo incorporation into the oxide crystalline structure is at its maximum. This temperature dependence is attributed to evaporation of the Mo species, which as previously shown, sublime at relatively low temperatures. Along the same lines, the Mo Raman vibrations for Mo:TiO_2-650 are relatively weak, which further confirms that the vast majority of Mo atoms are not incorporated in the TiO_2 lattice structure, instead they are impregnated on the surface of TiO_2 or distributed in interstitial sites of the TiO_2 structure, which agrees well with XRD patterns.

The composition and chemical state of Mo:TiO_2 films were further characterized by XPS. Fig. 5 shows the XPS high resolution spectra at the surface of Mo:TiO_2 samples. Ti 2p resolution spectra show the two characteristic peaks of Ti^{4+} in TiO_2 at 458 and 464 eV in the Mo:TiO_2 films.[42,48] The O 1s spectra for Mo:TiO_2 films are shown in Fig. 5b. The peak at lower binding energies mainly corresponds to crystal lattice oxygen O–Ti^{4+}, whereas the smaller peaks at higher binding energies correspond to hydroxyl groups or adsorbed water on the surface *i.e.* Ti–OH or Mo–OH.[42,48] Fig. 5c shows the high-resolution XPS surface spectra of Mo 3d. Surface Mo 3d spectra of all Mo:TiO_2 films show the characteristic peaks of Mo^{6+} situated at binding energies at 232 and 235 eV.[49–51] An additional doublet appears at lower binding energies for all Mo:TiO_2 films, attributed to the presence of some Mo^{5+} centers in the films.[52] XPS O 1s and Ti 2p spectra of TiO_2-650 are shown in Fig. S5 (ESI†). The binding energies for Ti 2p and O1s are in agreement with Mo:TiO_2 samples.

Electron paramagnetic resonance (EPR) spectroscopy was undertaken (at 120 K) to investigate the nature of the Mo doping within the series of TiO_2 lattice structures. EPR spectroscopy only detects the presence of paramagnetic species, thus the Mo^{5+} species are observed whereas there is no detection of Mo^{6+}
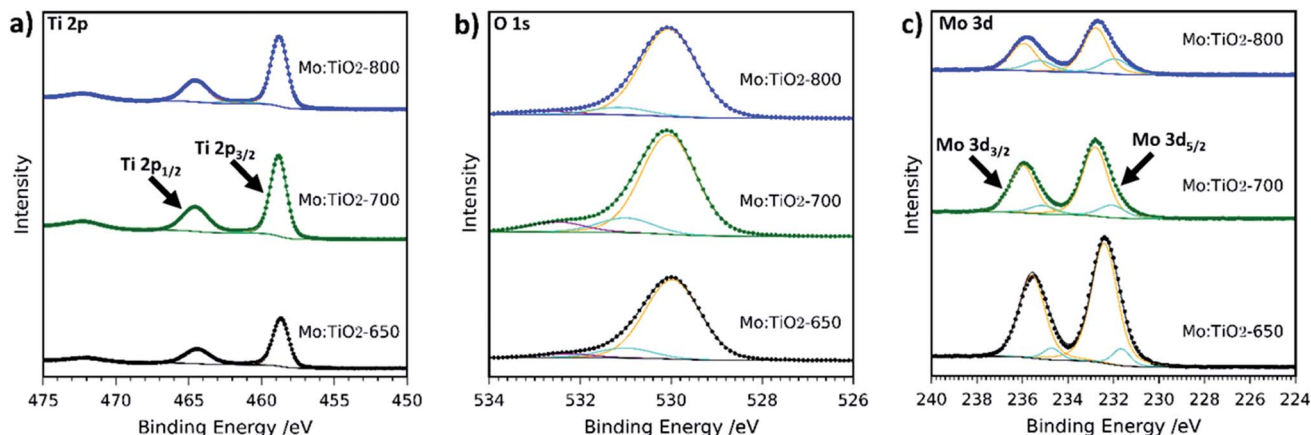
Fig. 5 XPS spectra of (a) Ti 2p, (b) O 1s and (c) Mo 3d of Mo:TiO$_2$. Scattered points correspond to raw data acquired in the measurements and solid lines to the fitted values.

centers. The EPR data (Fig. 6) indicates the presence of Mo^{5+} in all the films, in agreement with the XPS analysis. Variation in g values for the different samples demonstrated the existence of multiple Mo^{5+} species. As an example, the EPR spectrum of Mo:TiO$_2$-650 indicated the presence of MoO^{3+} species on the surface, characterized by an axial g-tensor ($g_\perp = 1.932$ and $g_\parallel = 1.886$) and corresponding weak hyperfine satellite lines originating from coupling of the unpaired electron to the two nuclear spin active isotopes of molybdenum (^{95,97}Mo, both with spin $I = 5/2$ and total natural abundance of 25.5%; $A_\perp = 112$ MHz and unresolvable $A_\parallel$). Additional contributions from bulk Mo^{5+} ($g_1 = 1.944$, $g_2 = 1.944$, $g_3 = 1.839$; $A_1 = 198$, $A_2 = 75$ and $A_3 = 93$ MHz) and a small contribution from Mo^{5+} in substitutional anatase lattice positions ($g_1 = 1.917$, $g_2 = 1.828$, $g_3 = 1.828$) was also detected in the Mo:TiO$_2$-650 sample. In contrast, the EPR spectra obtained for both the Mo:TiO$_2$-700 and Mo:TiO$_2$-800 samples confirmed the existence of substitutional and interstitial doping in the TiO$_2$ rutile lattice. The variation in Mo sites displayed *via* EPR for Mo:TiO$_2$-650 and both Mo:TiO$_2$-700 and Mo:TiO$_2$-800 confirms that substitutional doping mainly occurs in rutile TiO$_2$.

The particle size and crystallinity of Mo:TiO$_2$ were evaluated using TEM and SAED-TEM. Fig. 7 shows the corresponding SAED diffraction patterns, bright-field TEM and HRTEM images of Mo:TiO$_2$. To perform these analyses, a few milligrams of film deposited on FTO-ABS was scratched and dispersed in ethanol followed by TEM grid loading. The SAED-diffraction patterns (Fig. 7, 1st column) indicate a high polycrystalline character of these Mo:TiO$_2$ and TiO$_2$ particles. The corresponding diffraction pattern along with peak identification is shown in the inset of these figures. These data agree well with XRD where diffraction peaks corresponding to TiO$_2$ anatase and rutile are shown in Mo:TiO$_2$-650, Mo:TiO$_2$-700 and pure TiO$_2$, whereas only TiO$_2$ rutile is observed in Mo:TiO$_2$-800. Particle size distributions are shown in Fig. S6 (ESI†). In all Mo:TiO$_2$ samples, the particles possess a well-defined particle shape in comparison to pure TiO$_2$. Nevertheless, a large variability of particle sizes is observed in Mo:TiO$_2$-650 suggesting an insufficient annealing temperature for the formation of uniform particles. Mo:TiO$_2$-800 has the highest particle size due to aggregation and sintering of particles at high calcination temperatures.[53,54]

HRTEM images are shown in Fig. 7m–p. These images also reveal the highly crystalline character of Mo:TiO$_2$ and pure TiO$_2$. The measured lattice spacing for the TiO$_2$-650 sample agrees well with XRD analysis, since lattice spacings corresponding to the (101) diffraction plane of TiO$_2$ anatase and (101) of TiO$_2$ rutile are observed. In line with this, lattice spacings for Mo:TiO$_2$ also agree well with XRD and Raman analysis. More precisely, Mo:TiO$_2$-650 and Mo:TiO$_2$-700 show diffraction planes corresponding to both TiO$_2$ rutile and anatase crystalline phases, whereas only rutile TiO$_2$ particles are observed in Mo:TiO$_2$-800.

UV-Vis spectroscopy Tauc plots of Mo:TiO$_2$ and pure TiO$_2$ films are depicted in Fig. 8a and the corresponding absorption spectra are shown in Fig. S7 (ESI†). All Mo:TiO$_2$ samples exhibit lower band-gap energy values ranging from 2.6 to 2.7 eV compared to TiO$_2$-650, *ca.* 3.1 eV, being in accordance with literature reports.[7] The overall band-gap reduction for all Mo:TiO$_2$ is attributed to the incorporation of Mo$^{6+/5+}$ centers in

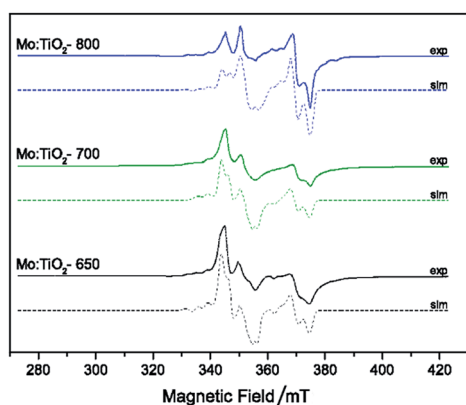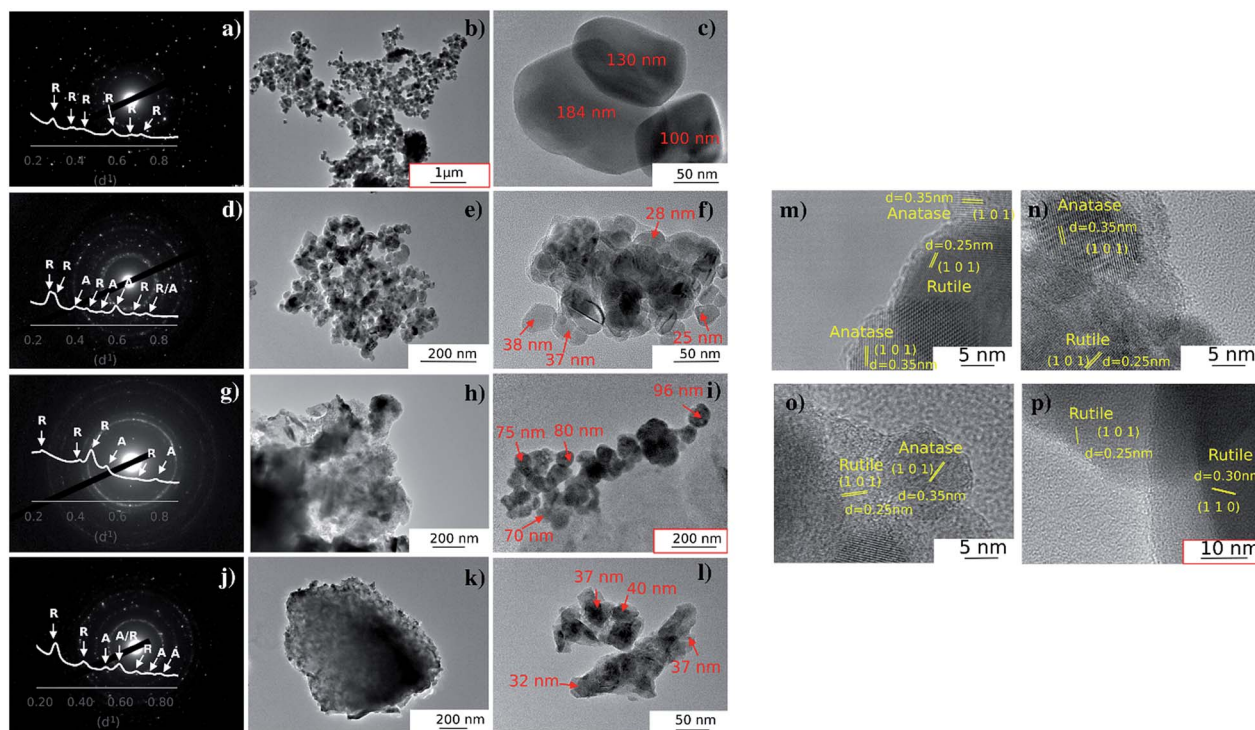**Fig. 6** CW X-band EPR spectra T ($T = 120$ K) of degassed samples at 393 K of Mo:TiO$_2$, experimental (solid line) and simulation (dashed-line).

Fig. 7 SAED-TEM diffraction patterns, TEM and HRTEM images: (a–c) Mo:TiO$_2$-800, (d–f) Mo:TiO$_2$-700, (g–i) Mo:TiO$_2$-650, (j–l) TiO$_2$-650, (m) TiO$_2$-650, (n) Mo:TiO$_2$-650, (o) Mo:TiO$_2$-700 and (p) Mo:TiO$_2$-800. For clarity, images (b), (i) and (p) do not have scales consistent with the rest.

the TiO$_2$ lattice structures, contributing to the formation of a shallow donor energy level below the CB of TiO$_2$.[47,55] Two distinguished slopes are observed for Mo:TiO$_2$-800. The lower energy one is related to the band gap, while the higher one we assign it to an Urbach tail caused by sample disorder (*i.e.* Ti–O, Ti–O–Mo bond breaking due to anatase transformation to rutile and Mo sublimation).[56]

The CB and VB position of TiO$_2$-650 and Mo:TiO$_2$ photo-anodes were determined using CV curves (Fig. S8, ESI†). Detailed information of the electrochemical characteristics of TiO$_2$ and Mo:TiO$_2$ are shown in Table S1 (ESI†). A schematic diagram of the relative position of CB and VB energy levels for

TiO$_2$-650 and Mo:TiO$_2$ samples is shown in Fig. 8b. Interestingly, in all Mo:TiO$_2$ samples the CB offset is narrowed down from approximately −3.01 eV for TiO$_2$-650 to *ca.* −4.2 eV for Mo:TiO$_2$. This further confirms that the incorporation of Mo$^{5+/6+}$ atoms at the TiO$_2$ lattice structure reduces the overall band-gap of TiO$_2$. The electrochemical band gap values obtained from CV curves are also shown in Table S1 (ESI†). The difference between the electrochemical band gap and optical band gap of TiO$_2$ and Mo:TiO$_2$ photoanodes is of 0.1–0.5 eV, which falls within the range of error.[57]

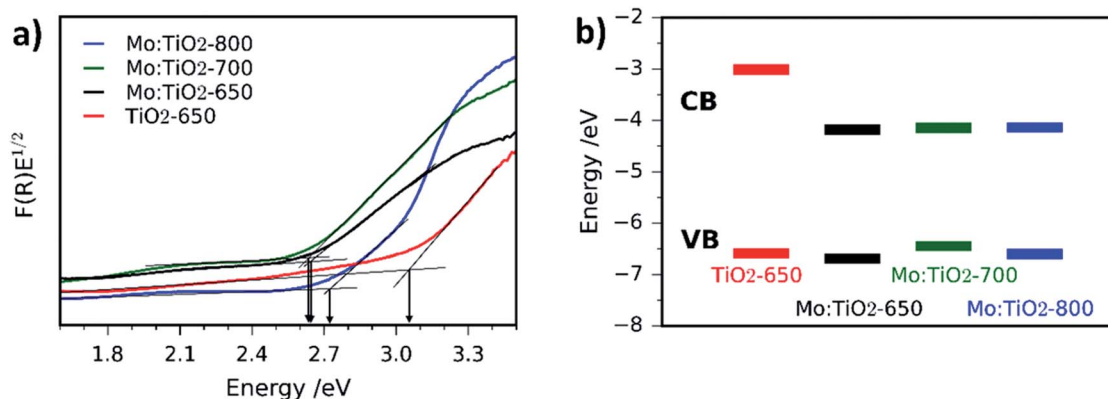The photocurrent density (at 1.23 V$_{RHE}$) as a function of annealing temperature for front illumination (*via* the

Fig. 8 Tauc plots of Mo:TiO$_2$-650, Mo:TiO$_2$-700, Mo:TiO$_2$-800 and pure TiO$_2$-650 photoanodes measured *via* diffuse reflectance UV-Vis spectroscopy. (b) Schematic diagram of CB and VB energy levels obtained by CV of Mo:TiO$_2$ and TiO$_2$ photoanodes.

electrolyte–film interface) and back illumination (*via* the ABS) was evaluated for Mo:TiO$_2$ and pure TiO$_2$ films and the results are shown in Fig. 9a. Photocurrent performances are higher when films are illuminated from the back, which indicates the porous photoanodes have a sufficient thickness. Fig. 9a also indicates that the optimal annealing temperature for pure TiO$_2$ is 650 °C (and for Mo:TiO$_2$ is 700 °C). In view of these results, all the following photoelectrochemical experiments were carried out directing the light towards the back of the photoelectrode (*via* the ABS) and using TiO$_2$-650 as a benchmark against Mo:TiO$_2$ films.

Photocurrent–potential (*J–V*) and photocurrent–time (*J–t*) curves are also shown in Fig. 9. *J–V* curves (Fig. 9b) under chopped simulated solar light indicate that Mo:TiO$_2$-700 outperforms the rest by almost a factor of two, reaching about 0.20 mA cm^{-2} at 1.23 V$_{RHE}$. This suggests that the annealing temperature has a significant effect. We assign this enhancement to a combination of (i) a smaller band gap, able to capture a higher fraction of the solar spectrum; (ii) higher surface area, as evidenced by FE-SEM and ESCA measurements (Fig. 2 and 3b); and (iii) to the presence of an anatase–rutile type-II heterojunction, that lowers the electron and hole recombination rate.[43,58–60] The slightly lower photocurrent observed for Mo:TiO$_2$ samples at lower applied bias in comparison to TiO$_2$-650 might arise from the different charge distribution at the space-charge region of Mo:TiO$_2$ that can affect the band-bending properties of the as-prepared photoanodes.[36] In fact, Z-potential

measurements of powdered suspensions of Mo:TiO$_2$ particles revealed a highly negatively charged surface at a broad pH range (pH 1–14). This highly negative surface may lead to the formation of an accumulation layer when the Mo:TiO$_2$ films are in contact with the electrolyte, requiring a larger applied bias to switch to a depletion layer and promote the migration of photocarriers.[36]

Two different co-catalysts, cobalt phosphate (Co-P$_i$) and CoFeO$_x$ have been evaluated in order to reduce the onset potential of Mo:TiO$_2$-700. Previous reports have shown that both co-catalysts are excellent candidates for reducing the onset potential owing to the decrease in electron–hole recombination at the electrode/electrolyte interface and reduction of surface charge recombination.[27,29,61] Fig. 9c shows the *J–V* curves for Mo:TiO$_2$-700 without co-catalyst and with either Co-Pi or CoFeO$_x$. Optimal deposition conditions were found to be 20 s of deposition time for CoP$_i$ loading and 3 cycles for CoFeO$_x$ (positively sweeping the voltage from 1.1 to 1.4 V$_{Ag/AgCl}$). Interestingly, both co-catalysts show a similar behaviour, where an enhancement in photocurrent is observed at low bias. At higher bias the driving force for the electron–hole separation comes from the higher applied bias itself rather than the co-cocatalyst, so main improvements with co-catalyst addition are only seen at low bias.[27]

Photocurrent–time curves at 1.23 V$_{RHE}$ also confirm that Mo:TiO$_2$-700 exhibits a twofold increase in photocurrent performance and reveals better photostability in comparison to
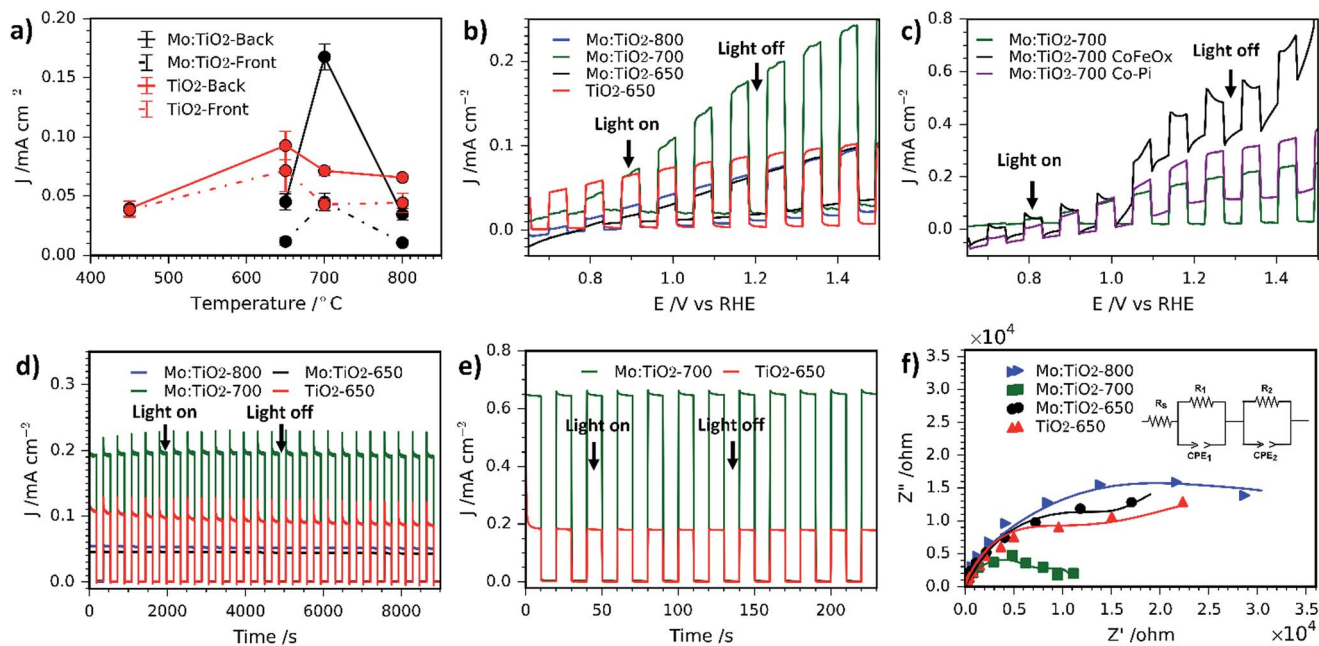

Fig. 9 (a) Variation of photocurrent density as a function of annealing temperature for Mo:TiO$_2$ and pure TiO$_2$ (at 1.23 V$_{RHE}$). Solid lines correspond to photoanodes where illumination was directed towards the back of the FTO-ABS and dashed-lines where illumination was directed towards the front of the working electrode. Error bars indicate standard error above and below the mean. (b) Photocurrent–potential curves of Mo:TiO$_2$ and pure TiO$_2$. (c) Photocurrent potential curves of Mo:TiO$_2$-700, Mo:TiO$_2$-700-CoFeO$_x$ and Mo:TiO$_2$-700-Co-Pi. (d) Photocurrent–time curves for 9000 s of Mo:TiO$_2$ and pure TiO$_2$ at an applied bias of 1.23 V$_{RHE}$. (e) Photocurrent–time curves for 250 s of Mo:TiO$_2$ and TiO$_2$-650 at an applied bias of 1.23 V$_{RHE}$ under UV illumination (365 nm, 3.6 mW cm^{-2}). (f) Nyquist plots of Mo:TiO$_2$ and pure TiO$_2$ in 1 M KOH. DC of 1.23 V$_{RHE}$; AC potential frequency range 10^5 to 0.01 Hz with an amplitude of 5 mV. The inset of the figure shows the equivalent circuit used to fit the data (solid lines). All electrochemical measurements were carried out in 1 M KOH aqueous electrolyte. All were irradiated with simulated sunlight (AM 1.5G, 100 mW cm^{-2}) except (e).

TiO_2-650 (Fig. 9d). The photostability for Mo:TiO_2 and TiO_2-650 photoanodes was quantified as the percentage of the photocurrent performance at the end of the last illuminated cycle (J) against the photocurrent performance at the end of the first illumination cycle (J_0), as previously reported by Paracchino et al.[62] After 9,000 s of chopped light irradiation, Mo:TiO_2-700 presented the best photostability with a J/J_0 of 99.0%, followed by Mo:TiO_2-650 ($J/J_0 = 95.7\%$), Mo:TiO_2-800 ($J/J_0 = 93.5\%$) and finally TiO_2-650 ($J/J_0 = 81.7\%$). Interestingly, all Mo:TiO_2 photoanodes resulted in an enhancement in the photostability in comparison to pure TiO_2, although only Mo:TiO_2-700 showed an improvement in the photocurrent performance over TiO_2-650. Unlike Mo:TiO_2-700, Mo:TiO_2-800 exhibits a lower photocurrent than TiO_2 at an applied bias of 1.23 V_{RHE}. This lower photocurrent performance is attributed to a combination of plausible reasons: first, Mo:TiO_2-800 only exhibits rutile TiO_2 in its composition due to the high annealing temperature employed for the preparation, as depicted in XRD and Raman experiments. Rutile TiO_2 is known to be less active than the anatase one, despite having a narrower band gap.[63] Second, unlike a rutile–anatase heterojunction where electrons and holes separate, the single phase rutile Mo:TiO_2-800 must suffer from higher electron–hole recombination.[43,58–60] Third, SEM images (Fig. 2) and ECSA measurements (Fig. 3b) also indicate a smaller surface area for Mo:TiO_2-800 with larger grains compared to Mo:TiO_2-700. Finally, many other factors such as particle size, aggregate shape and size may also influence the final photoelectrochemical performance of the Mo:TiO_2-800 film. In fact, TEM images showed higher particle size and aggregation for the Mo:TiO_2-800 photoanode, mainly due to the high annealing temperature employed.

Unlike Mo:TiO_2-800, Mo:TiO_2-650 shows both anatase and rutile TiO_2 crystalline phases, as demonstrated by XRD analysis and Raman spectroscopy and the measured band gap is considerably lower than pure TiO_2. Therefore, the poorer photoresponse behaviour of Mo:TiO_2-650 must be due to the type of Mo doping and to the film morphology. As shown in SEM-EDXS and XPS analyses, Mo:TiO_2-650 possesses the highest amount of Mo amongst the Mo:TiO_2 photoanodes and XRD analysis shows a small shift towards lower angles. This fact suggests that the clear majority of Mo$^{6+/5+}$ atoms are dispersed around the surface or occupying interstitial sites of the TiO_2 lattice structure, rather than occupying Ti^{4+} positions in the TiO_2 lattice structure. The presence of larger quantities of Mo$^{6+/5+}$ atoms on the surface of TiO_2 can reduce the photocurrent performance by creating recombination sites and blocking reaction sites.[6,7] Morphology and surface area can also play an important role in the photocurrent performance of photoanodes. As shown in the SEM images (Fig. 2j), very fine and poorly defined nanostructures are observed, which results in less surface area exposed for the water oxidation. This is further confirmed with ECSA measurements (Fig. 3b), where Mo:TiO_2-650 shows a significantly smaller surface area in comparison to Mo:TiO_2-700.

Photocurrent–time curves of Mo:TiO_2-700 and TiO_2-650 photoanodes at 1.23 V_{RHE} were also recorded using a UV lamp (365 nm, 3.6 mW cm^{-2}) and are shown in Fig. 9e. Under these conditions, Mo:TiO_2-700 also outperforms the performance of pure TiO_2, reaching a photocurrent value of ca. 0.65 mA cm^{-2} compared to ca. 0.2 mA cm^{-2}, respectively.

In order to further understand the enhancement in photoresponse for the Mo:TiO_2-700 photoanode, the charge transfer properties of photogenerated electrons and holes were studied using PEIS. Fig. 9f shows Nyquist plots of the as-prepared photoanodes recorded at a DC potential of 1.23 V_{RHE} under illumination and AC potential frequency range of 100000–0.01 Hz. The inset of Fig. 9f shows the equivalent circuit used to fit the Nyquist plots. It consists of an ohmic resistance and two RC elements in series, where R_s corresponds to the resistance of the cell, R_1 to the resistance of the electronic process in the bulk semiconductor along with Constant Phase Element 1 (CPE$_1$), and R_2 to the resistance of the interfacial charge transfer between the electrolyte and the photoanode along with CPE$_2$.[64] The corresponding fitted resistance values are listed in Table 1. As expected, the resistance values of the Mo:TiO_2-700 photoanode are smaller than that of Mo:TiO_2-650, Mo:TiO_2-800 and TiO_2-650, suggesting a better separation efficiency and faster transfer rate of photogenerated electrons and holes. This enhancement in the charge transfer properties of the Mo:TiO_2-700 photoanode agrees well with the J–t curves (Fig. 9d), that showed better photostability and a twofold photocurrent increase. This improvement is attributed to the presence of oxygen vacancies, formed to balance charges after partial doping with Mo$^{6+/5+}$. Oxygen vacancies are known to improve the electrical conductivity and charge transportation of TiO_2.[65,66] Since Mo:TiO_2-700 shows an optimal substitutional doping of Mo atoms into TiO_2, an enhancement in electron conductivity and charge transportation occurs, giving rise to higher photocurrents and stability.[65,66]

IPCE measurements for Mo:TiO_2-700 and pure TiO_2 photoanodes are shown in Fig. 10a. Pure TiO_2 values slowly increase from 0% at 500 nm to 1.4% at 400 nm and reach a maximum of 35% at 320 nm. However, Mo:TiO_2-700 IPCE values increase from 0% at 500 nm to 5% at 400 nm and reach a maximum of 40% at 330 nm. These IPCE results with monochromatic light confirm the superior performance of Mo:TiO_2-700 over pure TiO_2 on absorbing and utilizing visible light, and corroborate the photocurrent results and impedance analysis with polychromatic solar light.

O_2 evolution and photocurrent measurements were performed on Mo:TiO_2-700 at 1.23 V_{RHE} under 1 sun illumination for 340 min (Fig. 10b). The amount of O_2 in the headspace of the PEC cell increased linearly with time during irradiation. Using the photocurrent–time curve obtained (Fig. S9, ESI†), the theoretical amount of O_2 expected for a water oxidation reaction

Table 1 Calculated resistance parameters from EIS data

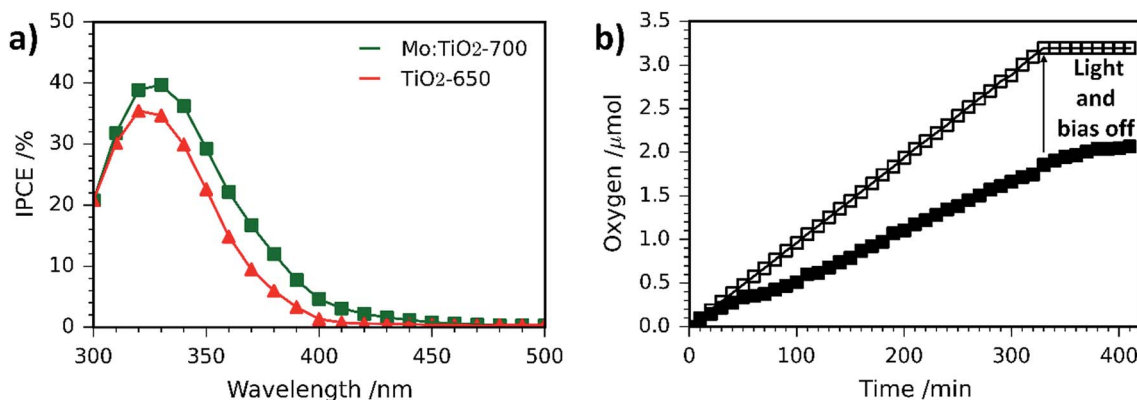| Sample	R_s (Ω)	R_1 (Ω)	R_2 (Ω)
Mo:TiO_2-650	11.99	10 098	64 870
Mo:TiO_2-700	13.11	1512	9902
Mo:TiO_2-800	12.07	10 098	36 055
TiO_2-650	11.77	6931	34 431

Fig. 10 (a) IPCE spectra at 1.23 V_{RHE} of Mo:TiO$_2$-700 and pure TiO$_2$. (b) Amount of O$_2$ gas evolved at 1.23 V_{RHE} under simulated sunlight (AM 1.5G, 100 mW cm^{-2}). The amount of O$_2$ quantified with a fluorescence probe is represented by solid markers, whereas the theoretical amount of O$_2$ calculated assuming a 100% faradaic efficiency is shown with empty markers.

with 100% faradaic efficiency was calculated and also represented in Fig. 10b. Comparison between values indicated that Mo:TiO$_2$-700 photoanode has a faradaic efficiency of approx. 60% (details of calculations are shown in ESI†). Similar efficiency values have been obtained on bare photoanodes without oxygen evolution electrocatalysts.[67]

4. Conclusions

In this work a facile and rapid approach for the design of Mo:TiO$_2$ photoanodes using a heterometallic oxo cage of the type [Ti$_4$Mo$_2$O$_8$(OEt)$_{10}$]$_2$ as a single source precursor has been demonstrated. The performance of the resultant photoanodes is highly reliant on the annealing temperature employed owing to its effects on the crystallinity, morphology and doping of TiO$_2$, being 700 °C the optimal annealing temperature. At this temperature, the Mo:TiO$_2$ photoanode (Mo:TiO$_2$-700) presents better photostability and a two-fold increase in photocurrent performance (0.20 mA cm^{-2} at 1.23 V_{RHE}) in comparison to a TiO$_2$ photoanode (0.10 mA cm^{-2} at 1.23 V_{RHE}). This improvement both in the photocatalytic performance and stability is attributed to a combination of several factors that become optimized at 700 °C: first, Mo:TiO$_2$-700 exhibits the presence of anatase TiO$_2$ and in minor amount rutile TiO$_2$, forming a heterostructure that is known to reduce the electron and hole recombination rate. Second, Mo:TiO$_2$-700 has a smaller band gap than the obtained at different annealing temperatures or without Mo doping, which allows for a better use of the solar spectrum and higher efficiencies (IPCE: 5% at 400 nm). Third, in Mo:TiO$_2$-700 there is preferred substitutional doping of Mo$^{6+/5+}$ atoms for Ti^{4+} atoms in the TiO$_2$ lattice structure, causing the presence of oxygen vacancies which improve the electrical conductivity and charge transportation of the film. Fourth, Mo:TiO$_2$-700 shows a large amount of cavities, porosity and well-defined nanostructures, resulting in the photoanode with the highest surface area. This characteristic morphology is associated to the spray pyrolysis deposition of [Ti$_4$Mo$_2$O$_8$(OEt)$_{10}$]$_2$ and to the partial sublimation of Mo species during the annealing process. On balance, these results clearly demonstrate a simple and effective methodology for preparing Mo-doped TiO$_2$ photoanodes with tuned electronic band properties and morphology and reveal the crucial parameters that allow the exploitation of heterometallic oxo cages in thin films for energy applications. These results open up the possibility for exploring a wide range of different heterometallic oxo cages for the fabrication of metal oxides photoanodes.

Conflicts of interest

There are no conflicts to declare.

Acknowledgements

References

1 K. Nakata and A. Fujishima, *J. Photochem. Photobiol., C*, 2012, **13**, 169–189.

2 M. Ni, M. K. H. Leung, D. Y. C. Leung and K. Sumathy, *Renew. Sustain. Energy Rev.*, 2007, **11**, 401–425.

3 A. Folli, J. Bloh, M. Strøm, T. Pilegaard Madsen, T. Hensriksen and D. E. Macphee, *J. Phys. Chem. Lett.*, 2014, **5**, 830–832.

4 R. M. Navarro, F. del Valle, J. A. Villoria de la Mano, M. C. Álvarez-Galván and J. L. G. Fierro, in *Advances in Chemical Engineering*, ed. B. S. R. Hugo I. de Lasa, Academic Press, 2009, vol. 36, pp. 111–143.

5 C. Sanchez, L. Rozes, F. Ribot, C. Laberty-Robert, D. Grosso, C. Sassoye, C. Boissiere and L. Nicole, *C. R. Chim.*, 2010, **13**, 3–39.

6 M. Kitano, M. Matsuoka, M. Ueshima and M. Anpo, *Appl. Catal., A*, 2007, **325**, 1–14.

7 M. Pelaez, N. T. Nolan, S. C. Pillai, M. K. Seery, P. Falaras, A. G. Kontos, P. S. M. Dunlop, J. W. J. Hamilton, J. A. Byrne, K. O'Shea, M. H. Entezari and D. D. Dionysiou, *Appl. Catal., B*, 2012, **125**, 331–349.

8 Y. Yan, J. Lee and X. Cui, *Vacuum*, 2017, **138**, 30–38.

9 W. Zhao, Y. Li, M. Zhang, J. Chen, L. Xie, Q. Shi and X. Zhu, *Chem. Eng. J.*, 2016, **283**, 105–113.

10 C. Wang, Z. Chen, H. Jin, C. Cao, J. Li and Z. Mi, *J. Mater. Chem. A*, 2014, **2**, 17820–17827.

11 Q. Liu, D. Ding, C. Ning and X. Wang, *Int. J. Hydrogen Energy*, 2015, **40**, 2107–2114.

12 S. Wang, L. N. Bai, H. M. Sun, Q. Jiang and J. S. Lian, *Powder Technol.*, 2013, **244**, 9–15.

13 O. Avilés-García, J. Espino-Valencia, R. Romero, J. L. Rico-Cerda, M. Arroyo-Albiter and R. Natividad, *Fuel*, 2017, **198**, 31–41.

14 Y. Yang, X. J. Li, J. T. Chen and L. Y. Wang, *J. Photochem. Photobiol., A*, 2004, **163**, 517–522.

15 B. Miljević, J. M. van der Bergh, S. Vučetić, D. Lazar and J. Ranogajec, *Ceram. Int.*, 2017, **43**, 8214–8221.

16 V. Štengl and S. Bakardjieva, *J. Phys. Chem. C*, 2010, **114**, 19308–19317.

17 T. Zhang, B. Yu, D. Wang and F. Zhou, *J. Power Sources*, 2015, **281**, 411–416.

18 P. D. Matthews, T. C. King and D. S. Wright, *Chem. Commun.*, 2014, **50**, 12815–12823.

19 Y. Lv, M. Yao, J. P. Holgado, T. Roth, A. Steiner, L. Gan, R. M. Lambert, D. S. Wright, E. Reisner, X. Liang, R. Li, Z. Xu and Q. Ren, *RSC Adv.*, 2013, **3**, 13659–13662.

20 Y. H. Lai, T. C. King, D. S. Wright and E. Reisner, *Chem.–Eur. J.*, 2013, **19**, 12943–12947.

21 J.-L. Hou, W. Luo, Y.-Y. Wu, H.-C. Su, G.-L. Zhang, Q.-Y. Zhu and J. Dai, *Dalton Trans.*, 2015, **44**, 19829–19835.

22 Y.-H. Lai, C.-Y. Lin, Y. Lv, T. C. King, A. Steiner, N. M. Muresan, L. Gan, D. S. Wright, E. Reisner, T. Da Ros, L. Casalis, A. Goldoni, M. Marcaccio, G. Scorrano, G. Scoles, F. Paolucci, M. Prato and M. Bonchio, *Chem. Commun.*, 2013, **49**, 4331–4333.

23 M. W. Kanan and D. G. Nocera, *Science*, 2008, **321**, 1072–1076.

24 S. Eslava, A. Reynal, V. G. Rocha, S. Barg and E. Saiz, *J. Mater. Chem. A*, 2016, **4**, 7200–7206.

25 S. Eslava, B. P. R. Goodwill, M. McPartlin and D. S. Wright, *Inorg. Chem.*, 2011, **50**, 5655–5662.

26 M. Ibadurrohman and K. Hellgardt, *Int. J. Hydrogen Energy*, 2014, **39**, 18204–18215.

27 G. Ai, R. Mo, H. Li and J. Zhong, *Nanoscale*, 2015, **7**, 6722–6728.

28 D. K. Zhong, M. Cornuz, K. Sivula, M. Grätzel and D. R. Gamelin, *Energy Environ. Sci.*, 2011, **4**, 1759–1764.

29 C. G. Morales-Guio, L. Liardet and X. Hu, *J. Am. Chem. Soc.*, 2016, **138**, 8946–8957.

30 B. K. Kang, G. S. Han, J. H. Baek, D. G. Lee, Y. H. Song, S. Bin Kwon, I. S. Cho, H. S. Jung and D. H. Yoon, *Adv. Mater. Interfaces*, 2017, **4**, 1700323.

31 Y. Duan, S. Zhou, Z. Chen, J. Luo, M. Zhang, F. Wang, T. Xu and C. Wang, *Catal. Sci. Technol.*, 2018, **8**, 1395–1403.

32 X. Jin, W. Sun, C. Chen, T. Wei, Y. Cheng, P. Li and Q. Li, *RSC Adv.*, 2014, **4**, 46008–46015.

33 Y. Li, H. Zhong, R. Li, Y. Zhou, C. Yang and Y. Li, *Adv. Funct. Mater.*, 2006, **16**, 1705–1716.

34 Z. Chen, Q. Li, C. Chen, J. Du, J. Tong, X. Jin, Y. Li, Y. Yuan, Y. Qin, T. Wei and W. Sun, *Phys. Chem. Chem. Phys.*, 2014, **16**, 24499–24508.

35 V. V. Pavlishchuk and A. W. Addison, *Inorg. Chim. Acta*, 2000, **298**, 97–102.

36 Z. Chen, H. N. Dinh and E. Miller, *Photoelectrochemical water splitting: standards, experimental methods, and protocols*, Springer-Verlag, New York, 2013.

37 S. Choopun, P. Mangkorntong, P. Subjareon, N. Mangkorntong, H. Tabata and T. Kawai, *Jpn. J. Appl. Phys.*, 2004, **43**, L91–L93.

38 D. A. H. Hanaor and C. C. Sorrell, *J. Mater. Sci.*, 2011, **46**, 855–874.

39 M. Lu, C. Shao, K. Wang, N. Lu, X. Zhang, P. Zhang, M. Zhang, X. Li and Y. Liu, *ACS Appl. Mater. Interfaces*, 2014, **6**, 9004–9012.

40 R. C. Pullar, S. J. Penn, X. Wang, I. M. Reaney and N. Mcn, *J. Eur. Ceram. Soc.*, 2009, **29**, 419–424.

41 W. M. Haynes, D. Lide and T. Bruno, *CRC handbook of chemistry and physics: A ready-reference book of chemical and physical data*, CRC Press, Taylor & Francis Group, 97th edn, 2016.

42 J. Yan, G. Wu, N. Guan, L. Li, Z. Li and X. Cao, *Phys. Chem. Chem. Phys.*, 2013, **15**, 10978–10988.

43 M.-C. Wu, P.-H. Lee and D.-L. Lee, *Int. J. Hydrogen Energy*, 2015, **40**, 4558–4566.

44 X. Du, L. Dong, C. Li, Y. Liang and Y. Chen, *Langmuir*, 1999, **15**, 1693–1697.

45 M. Dieterle and G. Mestl, *Phys. Chem. Chem. Phys.*, 2002, **4**, 822–826.

46 N. Illyaskutty, S. Sreedhar, G. Sanal Kumar, H. Kohler, M. Schwotzer, C. Natzeck and V. P. M. Pillai, *Nanoscale*, 2014, **6**, 13882–13894.

47 L. G. Devi and B. N. Murthy, *Catal. Lett.*, 2008, **125**, 320–330.

48 R. Sanjinés, H. Tang, H. Berger, F. Gozzo, G. Margaritondo and F. Lévy, *J. Appl. Phys.*, 1994, **75**, 2945–2951.

49 J. G. Choi and L. T. Thompson, *Appl. Surf. Sci.*, 1996, **93**, 143–149.

50 W. Zhou, Z. Yin, Y. Du, X. Huang, Z. Zeng, Z. Fan, H. Liu, J. Wang and H. Zhang, *Small*, 2013, **9**, 140–147.

51 Z. Chen, D. Cummins, B. N. Reinecke, E. Clark, M. K. Sunkara and T. F. Jaramillo, *Nano Lett.*, 2011, **11**, 4168–4175.

52 X. Xiao, T. Ding, L. Yuan, Y. Shen, Q. Zhong, X. Zhang, Y. Cao, B. Hu, T. Zhai, L. Gong, J. Chen, Y. Tong, J. Zhou and Z. L. Wang, *Adv. Energy Mater.*, 2012, **2**, 1328–1332.

53 W. Li, C. Ni, H. Lin, C. P. Huang and S. I. Shah, *J. Appl. Phys.*, 2004, **96**, 6663–6668.

54 Y. F. Chen, C. Y. Lee, M. Y. Yeng and H. T. Chiu, *J. Cryst. Growth*, 2003, **247**, 363–370.

55 Y. Gai, J. Li, S. S. Li, J. B. Xia and S. H. Wei, *Phys. Rev. Lett.*, 2009, **102**, 23–26.

56 B. Choudhury and A. Choudhury, *Phys. E*, 2014, **56**, 364–371.

57 K. Mahesh, S. Karpagam and F. Goubard, *eXPRESS Polym. Lett.*, 2018, **12**, 238–255.

58 Z. He, Q. Cai, H. Fang, G. Situ, J. Qiu, S. Song and J. Chen, *J. Environ. Sci.*, 2013, **25**, 2460–2468.

59 Z. Rui, S. Wu, C. Peng and H. Ji, *Chem. Eng. J.*, 2014, **243**, 254–264.

60 Y. Gao, H. Wang, J. Wu, R. Zhao, Y. Lu and B. Xin, *Appl. Surf. Sci.*, 2014, **294**, 36–41.

61 J. Zhang, R. García-Rodríguez, P. Cameron and S. Eslava, *Energy Environ. Sci.*, 2018, DOI: 10.1039/c8ee01346b.

62 A. Paracchino, V. Laporte, K. Sivula, M. Grätzel and E. Thimsen, *Nat. Mater.*, 2011, **10**, 456–461.

63 T. Luttrell, S. Halpegamage, J. Tao, A. Kramer, E. Sutter and M. Batzill, *Sci. Rep.*, 2014, **4**, 4043.

64 R. R. Devarapalli, J. Debgupta, V. K. Pillai and M. V. Shelke, *Sci. Rep.*, 2014, **4**, 1–8.

65 G. Wang, H. Wang, Y. Ling, Y. Tang, X. Yang, R. C. Fitzmorris, C. Wang, J. Z. Zhang and Y. Li, *Nano Lett.*, 2011, **11**, 3026–3033.

66 D. C. Cronzmeyer, *Phys. Rev.*, 1959, **113**, 1222–1226.

67 J. A. Seabold and K.-S. Choi, *Chem. Mater.*, 2011, **23**, 1105–1112.